Published in final edited form as:
IEEE Trans Med Imaging. 2011 March ; 30(3): . doi:10.1109/TMI.2010.2095027.

Diffeomorphic Image Registration of Diffusion MRI Using Spherical Harmonics

Xiujuan Geng,
Neuroimaging Research Branch, Intramural Research Program, National Institute on Drug Abuse, NIH, Baltimore, MD 21224 USA

Thomas J. Ross,
Neuroimaging Research Branch, Intramural Research Program, National Institute on Drug Abuse, NIH, Baltimore, MD 21224 USA

Hong Gu,
Neuroimaging Research Branch, Intramural Research Program, National Institute on Drug Abuse, NIH, Baltimore, MD 21224 USA

Wanyong Shin,
Neuroimaging Research Branch, Intramural Research Program, National Institute on Drug Abuse, NIH, Baltimore, MD 21224 USA

Wang Zhan,
Department of Radiology, University of California, San Francisco, CA 94121 USA

Yi-Ping Chao,
Department of Electrical Engineering, National Taiwan University, 106 Taiwan

Ching-Po Lin,
Institute of Neuroscience, National Yang-Ming University, 112 Taiwan

Norbert Schuff, and
Department of Radiology, University of California, San Francisco, CA 94121 USA

Yihong Yang
Neuroimaging Research Branch, Intramural Research Program, National Institute on Drug Abuse, NIH, Baltimore, MD 21224 USA

Xiujuan Geng: gengx@nida.nih.gov; Thomas J. Ross: tross@intra.nida.nih.gov; Hong Gu: hgu@intra.nida.nih.gov; Wanyong Shin: shinwa@nida.nih.gov; Wang Zhan: wang.zhan@ucsf.edu; Yi-Ping Chao: catpin@gmail.com; Ching-Po Lin: chingpolin@gmail.com; Norbert Schuff: norbert.schuff@ucsf.edu; Yihong Yang: yihongyang@intra.nida.nih.gov

Abstract

Non-rigid registration of diffusion MRI is crucial for group analyses and building white matter and fiber tract atlases. Most current diffusion MRI registration techniques are limited to the alignment of diffusion tensor imaging (DTI) data. We propose a novel diffeomorphic registration method for high angular resolution diffusion images by mapping their orientation distribution functions (ODFs). ODFs can be reconstructed using q-ball imaging (QBI) techniques and represented by spherical harmonics (SHs) to resolve intra-voxel fiber crossings. The registration is based on optimizing a diffeomorphic demons cost function. Unlike scalar images, deforming ODF maps requires ODF reorientation to maintain its consistency with the local fiber orientations. Our method simultaneously reorients the ODFs by computing a Wigner rotation matrix at each voxel, and applies it to the SH coefficients during registration. Rotation of the coefficients avoids the estimation of principal directions, which has no analytical solution and is time consuming. The proposed method was validated on both simulated and real data sets with various metrics, which include the distance between the estimated and simulated transformation fields, the standard

deviation of the general fractional anisotropy and the directional consistency of the deformed and reference images. The registration performance using SHs with different maximum orders were compared using these metrics. Results show that the diffeomorphic registration improved the affine alignment, and registration using SHs with higher order SHs further improved the registration accuracy by reducing the shape difference and improving the directional consistency of the registered and reference ODF maps.

Index Terms

Diffusion MRI; orientation distribution function (ODF); spherical harmonics; ODF reorientation; registration; diffeomorphisms

I. Introduction

Diffusion-based magnetic resonance imaging techniques have shown promises in the study of white matter microstructure and anatomical connectivity of the brain. Image registration is a crucial step for accurate group analyses of diffusion imaging data and for building white matter and fiber-tract atlases. With the assumption of a Gaussian distribution of the molecular diffusion, the second-order diffusion tensor imaging (DTI) [7] provides a relatively simple approach for quantifying diffusion anisotropy and for extracting local fiber directions. DTI-based registration methods have been developed to facilitate the alignment of DTI data [2], [45], [22], [41], [10], [28], [42]. However, a major drawback of DTI is that it may fail to accurately characterize the diffusion in complex white matter, where fiber tracts with different orientations intersect within an image voxel. Extension of DTI to high-angular resolution diffusion imaging (HARDI) has been proposed to characterize the apparent diffusion coefficient (ADC) profiles for the intravoxel fibers [35], [17], [1], [18], [38], [43], [44]. Methods using higher order tensors [5], [4], [23], [31], [27] and multi-tensor models [25], [24], [29] to quantify diffusivity profiles have also been introduced to solve this limitation. Another approach for solving intra-voxel fiber crossings is q-space imaging (QSI) [39], which measures the diffusion probability distribution function (PDF) by employing the Fourier transform relationship between the measured diffusion signals and the diffusion PDF. QSI is a 6-D imaging technique since the k-space encodes spatial positions and the q-space encodes diffusion displacements. Due to the sampling burden and large pulse gradient requirements, q-ball imaging (QBI) [34], [33] and hybrid diffusion imaging [40] techniques have been proposed. QBI samples the diffusion signals on a spherical shell and applies the Funk-Radon transform to reconstruct the model-free diffusion orientation distribution function (ODF) based on radial or spherical harmonic (SH) basis functions [20].

Systems with spherical symmetry are often more conveniently handled in a spherical basis. This leads to a natural representation of the local diffusion using SHs. SHs form an orthonormal basis for complex functions on a unit sphere and are widely used in various applications, such as shape modeling in molecular sciences and real-time lighting in computer graphics. Many diffusion decomposition and reconstruction techniques also use SHs [18], [20].

Several studies have been done to register HARDI data sets to take into account fiber crossing information during the registration. Barmpoutis *et al.* [6] proposed an affine registration method to map diffusivity profiles using 4th-order tensor models. Another work presented by Chiang *et al.* [11] performed the registration using spherical harmonics (SHs) by minimizing the Kullback-Leibler Divergence of the diffusivity profiles. The reorientation

was done by the "Preservation of Principal Directions (PPD)" method [2], and the principal directions were determined by the principal component analysis (PCA).

In this work, we propose a diffeomorphic registration method for HARDI data by mapping their ODFs represented using SHs. The potential advantage of ODF-based registration techniques is to align structures in locations where other image modalities are unable to characterize, for example, fiber crossings. This technique is not restricted to ODF registration; it can also be applied to align the apparent diffusion profiles represented by spherical harmonics.

The proposed registration method is based on optimizing an energy function including the ODF shape similarity cost defined with a L^2-norm and regularization constraints. The large deformation diffeomorphic framework was used to estimate smooth transformations between images with large shape differences. During the optimization, a rotation matrix is extracted at each voxel from the local Jacobian and converted to a general spherical harmonic rotation matrix to reorient the ODFs. The reorientation is directly applied to the coefficients without detecting principal directions ODFs which may have multiple directions and involve significant computation. Experimental results show that ODF reorientation makes the registered ODF shapes consistent with the local structures. Various metrics were defined and used to evaluate the proposed method on simulated and real diffusion data. The metrics include the distance between the estimated and the simulated transformation fields, the standard deviation of the general fractional anisotropy and the directional consistency of the deformed and reference images. The second order tensors and SHs contain the same amount of information. Therefore, the comparison of registrations using the second order and higher order SHs can be considered as the comparison of registrations using DTI and higher order models. Compared to second order SHs, registration using SHs with higher orders provides better performance in terms of smaller ODF shape difference and more consistent principal directions of the registered images.

II. Method

A. Diffusion ODFs Represented as Spherical Harmonics

The diffusion ODF characterizes the relative likelihood of water diffusion along any given angular direction **u** with $\mathbf{u}(\theta, \phi) = [\sin\theta\cos\phi \sin\theta\sin\phi \cos\theta]$ where θ and ϕ are the polar and azimuthal angles. The ODF, $F(\mathbf{u})$, is defined as the radial projection of the diffusion probability density function (PDF) $P(\mathbf{r})$: $F(\mathbf{u})=\int_0^\infty P(r\mathbf{u})dr$, where $\mathbf{r} = r\mathbf{u}$ is the relative spin displacement. $P(\mathbf{r})$ is related to the measured MR diffusion signal by the Fourier relationship, $P(\mathbf{r}) = \mathcal{F}(E(\mathbf{q}))$ [33]. $E(\mathbf{q})$ represents an underlying diffusion-attenuated signal at a finite set of points on a sphere and **q** is the wavevector defined as $\mathbf{q} = (2\pi)^{-1}\gamma\sigma g$, which describes diffusion encoding in a pulsed-gradient spin-echo experiment. Our registration method is applied to the reconstructed ODF maps from the QBI technique proposed by Hess *et al.* [20]. The ODF is approximated by a great circle integration on the sphere, i.e., $F(\mathbf{u})=\oint_{\mathbf{q}\perp\mathbf{u}} E(\mathbf{q})d\mathbf{q}$. As a single-valued spherical function, the function $F(\mathbf{u})$: $S^2 \to R^+$, can be represented as a linear combination of a set of spherical harmonic basis $Y_l^m(\mathbf{u})$ with order l and phase factor m: $F(\mathbf{u})=\sum_{l=0}^{L}\sum_{m=-l}^{l} C_l^m Y_l^m(\mathbf{u})$, where C_l^m denotes the harmonic series coefficient, and L is the maximum harmonic order. Since F is real, it is sufficient to utilize a real basis function set y_l^m, expanded as linear combinations of the complex harmonics:

$$y_l^m(\mathbf{u})=\begin{cases} Y_l^0(\mathbf{u}) & , \text{ if } m=0, \\ \frac{1}{\sqrt{2}}(Y_l^m(\mathbf{u})+(-1)^m Y_l^{-m}(\mathbf{u})) & , \text{ if } m>0, \\ \frac{i}{\sqrt{2}}((-1)^m Y_l^m(\mathbf{u})-Y_l^{-m}(\mathbf{u})) & , \text{ if } m<0. \end{cases} \quad (1)$$

F is also assumed to be antipodal symmetric, such that the order *l* only takes even numbers and the function can be expressed as

$$F(\mathbf{u})=\sum_{l=0,\,\text{even}}^{L}\sum_{m=-l}^{l} c_m^l y_l^m(\mathbf{u}), \quad (2)$$

where c_m^l represents the real harmonic series coefficient. In general, ODFs form an open subset of the space of L^2 spherical functions with the L^2 norm $\|F\|=\sqrt{<F,F>}$ [46]. In this work, we define the ODF shape difference with the L^2 norm. Given that the ODFs are represented with a complete set of orthonormal basis functions, they thus form a vector space analogue to unit basis vectors. The invariant shape norm and the distance between two functions can be defined as

$$\|F\|=\sqrt{<F,F>}=\sqrt{\sum_{l=0,\text{even}}^{L}\sum_{m=-l}^{l}\|c_m^l\|^2} \quad \text{and} \quad (3)$$

$$D(F_1,F_2)=\|F_1-F_2\|=\sqrt{\sum_{l=0,\text{even}}^{L}\sum_{m=-l}^{l}\|c_{1m}^l-c_{2m}^l\|^2} \quad (4)$$

The invariance of the basis functions simplifies the calculation of shape differences which can be performed using the corresponding coefficients as described in the above equation.

B. Rotation of Real Spherical Harmonics

A 3*D* rotation can be decomposed to three Euler angles using the *zyz* convention with three subsequent rotations around the *z*, *y* and *z* axes by angles α_1, α_2 and α_3, respectively: $\mathbf{R} = \mathbf{R}_Z(\alpha_3)\mathbf{R}_Y(\alpha_2)\mathbf{R}_Z(\alpha_1)$. For complex spherical harmonics, a rotation operator expressed in terms of the Euler angle parametrization can be represented with a Wigner matrix with the matrix elements given by [16]

$$\begin{aligned} D_{m'm}^l(\alpha_1,\alpha_2,\alpha_3)&=e^{-im'\alpha_1}d_{m'm}^l(\alpha_2)e^{-im\alpha_3}, \quad \text{where} \\ d_{m'm}^l(\alpha_2)&=\left[\frac{(l+m')!(l-m')!}{(l+m)!(l-m)!}\right]^{1/2} \\ \times\sum_{k=\max(0,m,-m')}^{\min(l-m',l+m)}&\left[(-1)^{k+m'-m}\begin{pmatrix} l+m \\ k \end{pmatrix}\times\begin{pmatrix} l-m \\ l-m'-k \end{pmatrix}\right. \\ &\left.\times(\cos\alpha_2/2)^{2l+m-m'-2k}(\sin\alpha_2/2)^{2k+m'-m}\right]. \end{aligned} \quad (5)$$

One can redefine the linear combination in Eq.(1) as $y_l^m(\mathbf{u})=\sum_{m'}A_{mm'}^l Y_{m'}^l(\mathbf{u})$, then the rotation matrix for real spherical harmonics is given by [30]

$$\mathbf{R}^l = A^l D^l A^{l\dagger}, \quad (6)$$

where † is the complex conjugate transpose. The coefficients of real spherical harmonics can be rotated in the same way as vectors with Wigner matrices. The coefficients λ_m^l for the rotated function $\mathbf{R}(F(\mathbf{u}))=\sum_l \sum_m \lambda_m^l y_l^m(\mathbf{u})$ can be represented as a linear transformation of the original coefficients:

$$\lambda_m^l(\alpha_1,\alpha_2,\alpha_3) = \sum_{m'=-l}^{l} R_{mm'}^l(\alpha_1,\alpha_2,\alpha_3) c_{m'}^l. \quad (7)$$

The Wigner matrix **R** is represented as a sparse block matrix:

$$\mathbf{R} = \begin{bmatrix} 1 & \mathbf{0} & \mathbf{0} & \cdots \\ \mathbf{0} & \mathbf{R^1} & \mathbf{0} & \cdots \\ \mathbf{0} & \mathbf{0} & \mathbf{R^2} & \cdots \\ \vdots & \vdots & \vdots & \ddots \end{bmatrix} \quad (8)$$

where $\mathbf{R}^l$ corresponds to the *l*th order. Note that rotation by *y*-axis mixes the spherical harmonic coefficients within an order, but not across order. To compute $\mathbf{R}_Y$, set α_1 and α_3 to be zero, and compute Eq.(5) and (6). The detailed implementation can be found in [30]. The *z*-axis rotation only changes the phase, which can be calculated as follows, without constructing $\mathbf{R}_Z$:

$$\lambda_m^l = c_{-m}^l \sin(-m\alpha) + c_m^l \cos(m\alpha). \quad (9)$$

C. Reorientation of Diffusion ODFs

Image registration searches for transformations to map structures in the source to corresponding ones in the reference. By assumption, the water diffusion orientation distributions reflect the underlying fiber structures; therefore, ODF reorientation along the transformation is required. The Jacobian of the spatial transformations is the first order linear approximation to the differentiable functions at a given spatial location. Therefore, an obvious approach is to apply the Jacobian to the ODF at each location to reorient it. Using this strategy, the shape and size of the ODFs are subject to change. To keep the shape invariant, we apply the rotation matrix extracted from the Jacobian to reorient the ODFs, which is similar to the "finite strain" tensor reorientation technique proposed by Alexander *et al.* [2]. A convenience of formulating ODFs with spherical harmonics is that the shape rotation can be achieved by applying a rotation matrix directly to the coefficients (see Sec.II-B) without changing the basis functions and reconstructing the ODFs after reorientation during each registration step.

D. Diffeomorphic Registration Framework

Our previous work [19] applied a small deformation elastic model to register diffusion MRI data sets. This type of registration can be generalized as a minimization problem of the following energy function:

$$E(\Phi) = E_{Sim}(I_1, I_2, \Phi) + E_{Reg}(u),$$

where Φ is the transformation field to be estimated that maps image I_1 to I_2, and $u = \Phi - I$ is the displacement field. A widely used similarity energy E_{sim} is the squared distance between intensities of the two images if they are scalars. The regularization energy E_{Reg} can be defined as $E_{Reg}(u) = \| \mathcal{L} u\|^2$ where $\mathcal{L}$ is a differential operator, e.g., the Laplacian operator. A limitation is that it prevents the target image from being fully deformed into the shape of the template image when a large deformation is needed to deform images.

Registrations with a large deformation model aim to solve this problem. “Viscous fluid” registration [13] estimates the transformations as the target image incrementally “flows” to the template image by minimizing

$$E(v^t)=E_{Sim}(I_1, I_2, \Phi^t)+E_{Reg}(v^t),$$

for any $t \in [0, 1]$, v^t is the velocity field at time t and $\Phi^t=\int_0^t v(\Phi(\tau), \tau)d\tau$. A recent large deformation diffeomorphic metric mapping (LDDMM) algorithm [8] searches the optimal transformation via solving the variational problem:

$$E(v^t)=E_{Sim}(I_1, I_2, \Phi)+E_{Reg}(v^t),$$

where $\Phi=\int_0^1 v(\Phi(t), t)dt$. These large deformation registration methods ensure that the estimated transformations are diffeomorphic, which are smooth invertible transformations with a smooth inverse, but require solving large sets of partial differential equations. A fast version of the diffeomorphic registration algorithm DARTEL [3] uses a multigrid approach and assumes a constant-velocity flow field along time. Another efficient method is called diffeomorphic demons [36], [37], which is an extension to the demons algorithms [32] and provides an efficient non-parametric diffeomorphic registration. Yeo [42] applied this framework to register DTI images with exact finite-strain differential.

A similar framework as diffeomorphic demons was performed in this work to estimate the large deformation transformation in diffeomorphisms. The overall optimization scheme is to separate the energy function into two parts by introducing another variable T, and estimate Φ and T alternatively at each iteration. The advantage is that optimization of a quadratic regularization form can be performed efficiently using a convolution kernel [9]. The energy function is defined as:

$$\begin{aligned} E&=E_{Sim}(F_1, F_2, \Phi^t)+D(\Phi^t, T^t)^2+E_{Reg}(T^t, v^t) \\ &=\sigma\int_\Omega \|F_1\circ\Phi^t(x)-F_2(x)\|^2dx+\rho\int_\Omega\|\Phi^t(x)-T^t(x)\|^2dx+\lambda_v\int_\Omega\mathcal{L}(v^t(x))^2dx+\lambda_T\int_\Omega\mathcal{L}(T^t(x))^2dx \end{aligned} \quad (10)$$

The second term is to constrain the separated T close to Φ. The last two terms are the regularization terms to ensure smooth velocity and transformation fields. We define $\mathcal{L}(\cdot)$ to be an isotropic differentiable operator $\nabla(\cdot)$. Then the optimization of Eq.(10), except the similarity term, can be done by convolving a Gaussian kernel K on v and T alternatively [9]. To minimize the first two terms, let $\phi^t = T^t \circ (I + v^t)$, and assume T^t is given, then the similarity term can be linearly approximated using a first-order Taylor expansion:

$$\begin{aligned} E_{sim}(v^t)&=\sigma\|(F_1\circ T^t-F_2)+\nabla F_1\circ T^t\cdot v^t+O(\|v^t\|^2)\|^2 \\ &\approx \sigma\|(F_1\circ T^t-F_2)+\nabla F_1\circ T^t\cdot v^t\|^2, \end{aligned}$$

and the first two terms become

$$E(v^t)=\sigma\|F_1\circ T-F_2+\nabla F_1\circ T^t\cdot v^t\|^2+\rho\|v^t\|^2 =\left\|\begin{bmatrix}\sqrt{\sigma}(F_1\circ T^t-F_2)\\0\end{bmatrix}+\begin{bmatrix}\sqrt{\sigma}\nabla F_1\circ T^t\\\sqrt{\rho}I\end{bmatrix}v^t\right\|^2 \quad (11)$$

The update of v^t can be calculated by setting the above equation to zero and solving for v^t:

$$v^t=\frac{-(\nabla F_1\circ T^t)'(F_1\circ T^t-F_2)}{\|\nabla F_1\circ T^t\|^2+\frac{\rho}{\sigma}I} \quad (12)$$

E. Implementation of Diffeomorphic Registration

We define the similarity cost using the shape difference metric in Eq.(4), and apply the ODF reorientation by the rotation matrix **R**. Then the similarity cost function can be rewritten as:

$$E_{sim}=\int_\Omega\|D(\mathbf{R}(F_1(\Phi^t(x))),F_2(x))\|^2dx =\int_\Omega\sum_{l=0,even}^{L}\sum_{m=-l}^{l}\|\lambda^l_{1m}(\Phi^t(x))-c^l_{2m}(x)\|^2dx, \quad (13)$$

where λ^l_m is the rotated coefficient defined in Eq.(7). The transformation fields are defined in Eulerian space, therefore the reorientation matrix operating on the deforming ODF should be extracted from the inverse Jacobian of the transformation $J^{-1}(\Phi)$, or from $J(\Phi)$ and taking the transpose afterwards:

$$\mathbf{R}=\left(\left(J(\Phi)\cdot J(\Phi)^T\right)^{-\frac{1}{2}}J(\Phi)\right)^T. \quad (14)$$

To apply the rotation to the spherical harmonic coefficients, **R** is decomposed into three Euler angles using the *zyz* convention. Let c_1 denote cos(α_1), s_1 denote sin(α_1), and define c_2, s_2, c_3 and s_3 accordingly. Then $\mathbf{R}(\alpha_1\alpha_2\alpha_3)$ is expressed as:

$$\begin{bmatrix}c_1c_2c_3-s_1s_3 & -c_2c_3s_1-c_1s_3 & c_3s_2\\c_3s_1+c_1c_2s_3 & c_1c_3-c_2s_1s_3 & s_2s_3\\-c_1s_2 & s_1s_2 & c_2\end{bmatrix} \quad (15)$$

Therefore, the three Euler angles are obtained as:

$$\begin{aligned}\alpha_1&=-\arctan(R_{32},R_{31}),\\\alpha_2&=-\arccos(R_{33}),\text{ and}\\\alpha_3&=\arctan(R_{23},R_{13}),\end{aligned} \quad (16)$$

with the constraints of $\alpha_1\in[-\pi\ \pi]$, $\alpha_2\in\left[-\frac{\pi}{2}\ \frac{\pi}{2}\right]$, and $\alpha_3\in[-\pi\ \pi]$. R_{ij} represents the element of **R** in the *i*th row and *j*th column, and (R_{ij},R_{kl}) represents the angle vector coordinate in the plane. Note that arctan(*a*, *b*) is almost equivalent to arctan(*a*/*b*) except that we also take into account the quadrant in which the point (a,b) is located.

The optimization of Eq.(10) is summarized in the Algorithm below. The details about choosing parameters are described in Sec.III-D.

Algorithm 1

Step 1	Initialize Φ^0 and T^0 to be identity fields.
Step 2	Compute the reoriented SH coefficients $\lambda_{1m}^{l}(\Phi^n)$ by extracting R according to Eq.(14), decomposing it into three angles using Eq.(16), and applying them to the coefficients using Eqs.(5), (6) and (9).
Step 3	Let $\Phi^n = T \circ (I + v^n)$. Estimate the velocity field v^{n+1} by minimizing Eq.(11), and the updated v^{n+1} is computed according to Eq.(12). After the computation of v^{n+1}, normalize it so that $\|v_{\max}^{n+1}\|=1$
Step 4	Regularize v by taking the Gaussian kernel of it: $v^{n+1} = \lambda_v K * v^{n+1}$
Step 5	Let $T^{n+1} = \lambda_T K * T^n \circ (I + v^{n+1})$, and $\Phi^{n+1} = T^{n+1}$
Step 6	repeat steps 2–5 until convergence, $E_{Sim} < \varepsilon$, or $n > N_{max}$.

Technically, $\lambda(\cdot)$ in Eq.(13) is itself a function of the deformation field, therefore the update of v^t in Eq.(12) does not fit exactly. In this work, however, we followed the demons implementation and ignored the exact differential of the ODF reorientation. This approximation was made since taking care of reorientation in ODF is much more complicated than in DTI [42].

III. Experiments and Results

A. Data Acquisition and Preprocessing

Human brain QBI data from five healthy subjects were acquired on a 3T TrioTim Siemens MRI scanner. Each subject was scanned twice with a short out-of-scanner break between the two sessions. Isotropic axial diffusion-weighted images (DWIs) were obtained using a single shot diffusion spin-echo echo-planar imaging (EPI) sequence with TR/TE = 8,000/114 ms, FOV= 195 mm, and matrix size = 78×78, yielding a 2.5mm image resolution. Using an electrostatic repulsion model, 162 diffusion encoding directions with a b value of 3000 s/mm^2 and one reference image with $b = 0$ were acquired. Sixty slices with slice thickness of 2.5mm were obtained to cover the whole brain. The total scan time was approximately 26 minutes.

The non-brain regions were masked out using AFNI [15] based on the baseline DWIs at $b = 0$, instead of a DWI at $b = 3000$ due to its relatively low SNR. ODF maps were then reconstructed as described in [20]. All 10 b0 maps (five subjects, each subject contains two sessions) were first shifted to align the volume centers, and then averaged. Each b0 map was affine aligned to the average b0 map using the Hellinger metric, the square root of Jensen-Shannon divergence. The affine matrices were then applied to the corresponding SH coefficients. The rotation was done by extracting the rotation matrix from the matrix and applying on the coefficients similar as Step 2 in Alg.1. Linear interpolation of the SH coefficients was used throughout the preprocessing and registration steps.

B. Diffusion ODF Represented by SH Coefficients

ODFs represented by SHs with maximum order L require $(L+1)\times(L+2)/2$ number of coefficients. Registration using coefficients reduces the computation cost compared to using the sample points on diffusion MRI images. We use the SH coefficients of non-normalized ODF maps as input. Fig. 1 shows an example diffusion data set. The ODF was computed using $F(\mathbf{u}) = \oint_{\mathbf{q}\perp\mathbf{u}} E(\mathbf{q}) d\mathbf{q}$. The norm of the non-normalized SH coefficients is proportional to the summation of the diffusion weighted signal $E(q)$. The contrast was significantly

reduced after ODF normalization. The non-normalized SH norms have consistent histograms across subjects (Fig. 2(a)) given the same set of acquisition parameters, so that the simple intensity difference metric can be used as the similarity cost for registration. Therefore, we chose the non-normalized ones to define the energy function. The majority of the energy of a SH shape can be represented by its lower order coefficients. The bottom row of Fig. 1 shows ODF coefficients at orders of of 0, 2, 4, 6 and 8 where all orders except order 0 share the same color scale. Fig. 2(b) plots the histogram of different levels of coefficients over an ODF map.

C. Synthetic Experiments of Reorientation

Diffusion tensors with three zero-mean Gaussians under a low intravoxel water exchange model were simulated with a SNR of 100 using "Camino" [14]. The largest eigenvalues of the three tensors were set to be $3\times10^{-9}m^2/s$, $2\times10^{-9}m^2/s$ and $1.5\times10^{-9}m^2/s$ along the x, y and z axes, respectively. The other two eigenvalues had a value of $0.6\times10^{-9}m^2/s$ along the *y* and *z* axes, the *x* and *z* axes, and the *x* and *y* axes. 162 encoding directions were used for the QBI acquisition with $b = 3000\ s/mm^2$. Fig. 3(a) shows the reconstructed ODF projected on the *xy* and the *xz* planes. The 3D visualization was implemented using Python. 30° rotations along the *z* and *y* axes were applied separately on the spherical harmonic coefficients according to Eqs.(5), (6), and (9). Fig. 3(b) plots the coefficients of the original and rotated ODFs.

Fig. 4 demonstrates a spatial rotation of 25° of a real diffusion data set with and without ODF reorientation. A rotation transformation without ODF reorientation resulted in an inconsistency between the principal directions of the ODFs and the underlying fiber directions. With ODF reorientation of the coefficients, the principal directions were rotated to follow the transformed fiber structures.

To test the orientational consistency between two ODF shapes, a directional consistency (DC) metric was used. Given two spherical shapes, search for an angle α so that $\|R(\alpha)(F_1) - F_2\|^2$ is minimized, and define $|\cos(\alpha)|$ to be the measure of the DC between the two shapes. In this work, we applied an exhaustive search to compute the DC. First decompose the arbitrary rotation $R(\alpha)(F) = R_Z(\alpha_3)R_Y(\alpha_2)R_Z(\alpha_1)(F)$, set the coarse searching step to be 10_o, and search the angles, $\alpha_1, \alpha_2, \alpha_3 \in [-\pi, \pi]$, that minimized the shape difference. Then use them as the initialization, set the fine searching step to be 1°, and search the rotation angles in the domain of $\alpha_i \in [\alpha_i^{initial} - 10^o, \alpha_i^{initial} + 10^o]$, $i = 1, 2, 3$. We get (see Appendix for the derivation):

$$DC = |cos(\alpha)|$$
$$= 0.5(4 - ((R(2,1) - R(1,2))^2 + (R(1,3) - R(3,1))^2 + (R(3,2) - R(2,3))^2))^{\frac{1}{2}}.$$

To test the accuracy of the metric, we computed the DC for each voxel between the reoriented and non-reoriented ODF maps. The DC map is shown in Fig. 4. The average DC value was 0.9096, corresponding to 24.55°, which is close to the real rotation angle 25°.

D. Validation with Simulated Transformation

We synthesized images with known transformations and applied the proposed method to select proper weighting parameters, validate the reorientation, and test the performance using SHs with different maximum orders.

A set of deformation fields were simulated by generating sine functions: $f = (a \sin(5\pi y), b \sin(5\pi x), 0)$, where $x, y \in [0, 1]$. We set $a = 2, 3, 4$ to simulate three fields with various

amplitudes. Then a real diffusion image was randomly selected and deformed using the three fields to generate synthesized reference images.

1) Parameter Evaluation—Similar to Yeo *et al.*'s approach [42], we set the similarity weight parameter $\sigma=\frac{1}{\|F_1\circ T^t-F_1\|^2}$, and kept the update field v^t to be less than 1 voxel at each iteration by changing ρ. To select proper weight parameters for the regularization terms, we set $\lambda_T = 0$, and varied λ_v from 0.2 to 2. A proper λ_v was chosen so that the overall registration error including the similarity error and regularization cost is small. The similarity error is defined by $\frac{1}{V_\Omega}\int_\Omega \|F_1\circ T^t(x)-F_1(x)\|^2 dx$, and the regularization cost is defined by $\frac{1}{V_\Omega}\int_\Omega \|\nabla(T^t-x)\|^2$, where V_Ω is the total volume of the integrated region. Then λ_T was varied from 0.2 to 2, and a proper λ_T was chosen according to the same rule. Fig. 5 plots the similarity error and regularization cost during the registration for different parameter settings. A multi-resolution scheme was used during the registration. The images were down-sampled to $\frac{1}{4}\times\frac{1}{4}\times\frac{1}{4}$, and $\frac{1}{2}\times\frac{1}{2}\times\frac{1}{2}$ at the coarse levels to register larger structures, and then were registered at the full resolution to map finer shapes. We chose λ_v = 1.0 and λ_T = 0.5 to keep the similarity error and regularization cost relatively low. The same set of parameters were used to register the real images throughout the paper. Fig. 6(b) shows the estimated transformation fields under λ_T = 0, λ_v = 0.5; λ_T = 0.5, λ_v = 1.0; and λ_T = 1.0, λ_v = 1.0. The field generated by λ_T = 0 is over deformed in some regions, whereas λ_T = 1.0 produced an overly smooth field.

2) Effect of SH Coefficients with Different Maximum Orders—To study the effect of registrations with different SH orders, the diffusion images were reconstructed with L = 2, 4, 6, 8. The proposed method is general to any order of SHs. Since the second order tensor model can be represented using SHs with L = 2, registration based on tensor models and SHs with L = 2 contain the same amount of information. Fig. 6 shows a registration example using the simulated sine transformation with a = 3. Fig. 6(d) and (e) show the simulated and registered ODF shapes using SHs with L = 2, 4, 6, 8 in the box region. The second order model does not contain fiber crossing information, while the higher orders can describe orientation distributions with multiple peaks. The ODF shapes after the same registration but without ODF reorientation were shown in Fig. 6(f). The directions do not match those in the reference image, whereas the directions of the ODFs with ODF reorientation are consistent to the reference.

Three metrics were used to measure the performance. One is the normalized distance between the estimated deformation field and the "ground truth" deformation field from the simulation. The second one is the normalized standard deviation of the generalized fractional anisotropy (GFA). The third one is the directional consistency. Similar to the FA used in DTI studies, GFA is a shape index of the ODF and defined as [33]:

$$GFA=\sqrt{\frac{n\sum_{i=1}^{n}(F(\mathbf{u}_i)-F_{ave})^2}{(n-1)\sum_{i=1}^{n}F(\mathbf{u}_i)^2}},$$

where n is the number of reconstructed samples (246 in this paper) of the ODF and $F_{ave}=\frac{1}{n}\sum_{i=1}^{n}F(u_i)$. The normalized standard deviation of the GFA was computed between the average and the deformed ODF maps following the equation:

$$nSTD_{GFA}(x)=\frac{\sqrt{\sum_{i=1}^{N-1}(GFA(F_i(\Phi(x)))-GFA(\overline{F}(x)))^2}}{(N-1)\cdot GFA(\overline{F}(x))}, \quad (17)$$

where $\overline{F}(x)=\frac{1}{N}\sum_{i=1}^{N}F_i(x)$, F_N is the reference, and the other $N-1$ ODF maps are registered to F_N. The average field distance, nSTD of GFA and DC over a mask by thresholding the reference GFA map at 0.1 are shown in Table I. Using higher order SHs improved the registration performance in terms of reducing the field distance and standard deviation of the GFA, and increasing the DC. However the improvement percentage is low, likely because that the higher order coefficients account for a small portion of the overall energy. The field distance is about half of the simulated distance. The difference map between the reference and the registered ODF norm using $L = 4$ is shown in Fig. 6(c), which is very close to zero. The average error was 0.0083 over the mask with the GFA > 0.1.

E. Registration of Real Diffusion Images

After preprocessing, all diffusion images were affine aligned to their average making them ready for the diffeomorphic registration. Each ODF map was reconstructed by four sets of SHs with $L = 2, 4, 6, 8$. One image was selected as the reference, and nine other images were registered to it using the proposed registration method. The registration was repeated four times. Each time corresponded to the SH coefficients with a different L. Since each subject was scanned twice, the intra-subject registration was done to provide a upper limit of the registration performance. Fig. 7 shows the ODF maps using the norm of the SH coefficients with L=4 after affine alignment and diffeomorphic registration, and the absolute difference between the reference and the registered ODF maps. The intrasubject registration has close to zero difference between the ODF norms. However there are still errors in the ventricles, and in cortical regions. The inter-subject diffeomorphic registration was a significant improvement over affine alignment, and provided a relatively small ODF shape difference.

Two metrics were computed for evaluation: the normalized standard deviation of the GFA defined in Eq.(17); and the DC between the reference and each deformed ODF maps. A mask with the reference GFA > 0.1 was used for computing the GFA, and its intersection with more than two principal directions was used for the average DC. Principle directions were computed at each voxel in the reference image using “Camino” [14]. Fig. 8 plots the histograms of the metrics using SHs with different maximum orders. Registrations with higher orders reduced the standard error of the GFA, and therefore reduced the shape difference between the registered and reference ODF maps. The deformed ODF directions, over regions with multiple principal directions, were more consistent with the reference ODF shapes using registration with higher order SHs compared to the second order SHs. There was little difference in the DC when using SHs with $L > 2$.

To test the method and order effects, we did two-factor repeated measures ANOVA on the two metrics separately. The two factors were method (affine and diffeomorphic) and order (L=2, 4, 6, 8). The analysis was first applied to the average difference GFA values between the deformed and reference ODFs normalized by the reference GFA. There were main effects of method with $F(1,4)=488.442$; $p < 0.001$ and order with $F(3,12)=3389.895$; $p < 0.001$, and an interaction between method and order with $F(3,12)=209.285$; $p < 0.001$. Post-hoc analyses showed that there were significant differences between any two different orders and the higher orders produced smaller GFA difference. The same ANOVA was then performed on the average DC between the deformed and reference ODF maps. There were main effects of method with $F(1,4)=13.578$; $p < 0.021$, and order with $F(3,12)=237.122$; $p <$

0.001, and an interaction between these two with $F(3,12) = 4.345$; $p < 0.027$. Post-hoc analyses showed that there were significant differences only between order 2 and any other higher orders. Fig. 9 plots the mean and standard errors of the metrics with different methods and orders. In general, the diffeomorphic registration methods significantly reduced the ODF shape difference and improved directional consistency compared to the affine methods. The shape difference can be further reduced by increasing the maximum orders. Registrations with $L \geq 2$ improved the directional consistency compared with $L = 2$, but no more improvements were found by further increasing the order.

The registration computation time was about 6 minutes with L=2, 10 minutes with L=4, 22 minutes with L=6 and 50 minutes with L=8. All real data registrations data were implemented following a 3-level multi-resolution registration scheme: $\frac{1}{4} \times \frac{1}{4} \times \frac{1}{4}$ resolution with 50 iterations, $\frac{1}{2} \times \frac{1}{2} \times \frac{1}{2}$ resolution with 50 iterations, and full resolution with 20 iteration. The image dimension is 78 ×78 ×48 and all registrations were run on a 2.4 GHz AMD Opteron Linux system.

IV. Discussion

The registration performance improvement using SHs with higher orders compared to the second order can be explained in that the higher order coefficients provide more information in fiber crossing regions, and this additional information helps the registration to better align the ODF shapes and therefore better align the local structures to the corresponding ones in the reference. Complex structures such as crossing fibers occur not only in white matter, but also in gray matter. Therefore, compared to tensor based methods, registrations using higher order models have the potential to better align white and gray matter regions.

Unlike scalar based registrations, vector-based registrations require reorientation of the vectors when deforming the images. Chiang *et al.* [11] proposed a reorientation method that first detected the principal direction of the diffusivity functions by shape-based PCA, and then applied PPD to reorient the diffusivity function. A major difference of our approach is that, instead of computing the diffusion attenuation signal at each reoriented direction, we apply the rotation matrices directly to the coefficients to get the reoriented ODF. As QBI techniques normally acquire several hundred sampling directions, performing operations on much fewer coefficients reduces the computation cost significantly. The calculation of the rotation matrix $\mathbf{R}_Y$ is relatively computationally intensive compared to $\mathbf{R}_Z$. A fast spherical harmonic rotation approximation using a truncated Taylor expansion of $\mathbf{R}_Y$ [26] can be used to speed up the calculation, however the accuracy is compromised.

Although there were significant improvement of the shape similarity and directional consistency when increasing the SH order, the percentage improvement is small. This may be due to the relatively insensitive shape metric to the higher orders. In this work, we define the ODF shape difference with the L^2 norm. The same weight factors were given to the 0-order and other order coefficients. Metrics more sensitive to rotation and higher order coefficients would potentially magnify the improvement. An alternative metric, the Kullback- Leibler Divergence introduced by Chiang *et al.* [11], [12], can also be applied to define the shape similarity.

Due to the relatively low SNR (around 10) in QBI data, in many white and gray matter regions the ODF peaks may not truly reflect the underlying structures. The peaks in those regions between source and reference have large differences to begin with and are hard to match even with ODF reorientation. This may explain the results that, when increasing the SH order from four to higher ones, the improvement of the directional consistency was not significant.

The calculation of the differential of the ODF reorientation is ignored in this work as we mentioned in Sec. II-E. Taking it into account may improve the registration performance [42]. We only considered to reorient ODFs using rotation matrices during the registration procedure. The transformation of ODFs may be further improved by accounting for shearing effect [21]. Another limitation of the proposed ODF-based registration is that it fully depends on the quality of the reconstructed ODF maps. Metrics derived from other models (such as fractional anisotropy from DTI) may help to validate the registration performance and analyze how much the reconstructed ODF would affect the registration results.

V. Conclusions

We presented a diffeomorphic diffusion MRI registration algorithm based on the reconstructed ODFs represented by spherical harmonics. The ODF reorientation was performed during the registration procedure. The reorientation matrices were obtained by extracting the rotation part from the local Jacobian and directly applied to the spherical harmonic coefficients. Computation of the principal directions and reconstruction of the ODFs during each registration iteration are avoided. The similarity cost was computed based on a shape difference metric defined using the L^2 norm of the SH coefficients. The diffeomorphic deformation framework makes the registration suitable to map images with large shape differences. ODF reorientation was tested using synthetic and real q-ball data with known rotation angles and simulated transformation fields. The registration method was evaluated using the field distance metric, the normalized standard deviation of the GFA and the average directional consistency. Registrations using SHs with different maximum orders were compared using both simulated and real data. Results show that higher order SHs reduced the ODF shape difference and improved directional consistency compared to lower order SHs.

Acknowledgments

This work was supported by the Intramural Research Program of the National Institute on Drug Abuse (NIDA), National Institute of Health (NIH).

References

1. Alexander D, Barker G, Arridge S. Detection and modeling of non-gaussian apparent diffusion coefficient profiles in human brain data. Magnetic Resonance in Medicine. 2002; 48(2):331–340. [PubMed: 12210942]
2. Alexander D, Pierpaoli C, Basser P, Gee J. Spatial transformations of diffusion tensor magnetic resonance images. IEEE Trans Med Imaging. 2001; 20(11):1131–1139. [PubMed: 11700739]
3. Ashburner J. A fast diffeomorphic image registration algorithm. NeuroImage. 2007; 38:95–113. [PubMed: 17761438]
4. Barmpoutis A, Hwang MS, Howland D, Forder JR, Vemuri BC. Regularized positive-definite fourth order tensor field estimation from dw-mri. NeuroImage. 2009; 45:S153–S162. [PubMed: 19063978]
5. Barmpoutis A, Jian B, Vemuri1 BC, Shepherd TM. Symmetric positive 4th order tensors & their estimation from diffusion weighted mri. Information Processing in Medical Imaging. 2007:308–319. [PubMed: 17633709]
6. Barmpoutis A, Vemuri BC, Forder JR. Registration of high angular resolution diffusion mri images using 4th order tensors. MICCAI. 2007:908–15. [PubMed: 18051145]
7. Basser PJ, Pierpaoli C. Microstructural and physiological features of tissues elucidated by quantitative-diffusion-tensor mri. Journal of Magnetic Resonance. 1996; 111:209–219. vol. Series B. [PubMed: 8661285]
8. Beg MF, Miller MI, Trouve A, Younes L. Computing large deformation metric mappings via geodesic flows of diffeomorphisms. International Journal of Computer Vision. 2005; 61(2):139–157.

9. Cachier P, Ayache N. Isotropic energies, filters and splines for vector field regularization. Journal of Mathematical Imaging and Vision. 2004; 20(3):251–265.
10. Ceritoglu C, Oishi K, Li X, Chou MC, Younes L, Albert M, Lyketsos C, van Zijl PC, Miller MI, Mori S. Multi-contrast large deformation diffeomorphic metric mapping for diffusion tensor imaging. NeuroImage. 2009; 47:618–627. [PubMed: 19398016]
11. Chiang M, Klunder A, McMahon K, de Zubicaray G, Wright M, Toga A, Thompson P. Information-theoretic analysis of brain white matter fiber orientation distribution functions. Information Processing in Medical Imaging. 2007:172–182. [PubMed: 17633698]
12. Chiang MC, Leow AD, Klunder AD, Dutton RA, Barysheva M, Rose SE, McMahon KL, de Zubicaray GI, Toga AW, Thompson PM. Fluid registration of diffusion tensor images using information theory. IEEE Trans Med Imaging. 2008; 27(4):442– 456. [PubMed: 18390342]
13. Christensen G, Rabbitt R, Miller M. Deformable templates using large deformation kinematics. IEEE Trans Image Proc. Oct; 1996 5(10):1435–1447.
14. Cook, PA.; Bai, Y.; Nedjati-Gilani, S.; Seunarine, KK.; Hall, MG.; Parker, GJ.; Alexander, DC. Camino: Open-source diffusion-mri reconstruction and processing. 14th Scientific Meeting of the International Society for Magnetic Resonance in Medicine; 2006.
15. Cox RW. AFNI: Software for analysis and visualization of functional magnetic resonance neuroimages. Computers and Biomedical Research. 1996; 29:162–173. [PubMed: 8812068]
16. Edmonds, A. Angular Momentum in Quantum Mechanics. Princeton University Press; 1996.
17. Frank LR. Anisotropy in high angular resolution diffusion-weighted mri. Magnetic Resonance in Medicine. 2001; 45(6):935–939. [PubMed: 11378869]
18. Frank LR. Characterization of anisotropy in high angular resolution diffusion-weighted mri. Magnetic Resonance in Medicine. 2002; 47(6):1083–1099. [PubMed: 12111955]
19. Geng X, Ross TJ, Zhan W, Gu H, Chao Y-P, Lin C-P, Christensen GE, Schuff N, Yang Y. Diffusion mri registration using orientation. Information Processing in Medical Imaging. 2009:626–637. [PubMed: 19694299]
20. Hess C, Mukherjee P, Han E, Xu D, Vigneron D. Q-ball reconstruction of multimodal fiber orientations using the spherical harmonic basis. Magnetic Resonance in Medicine. 2006; 56:104–117. [PubMed: 16755539]
21. Hong X, Arlinghaus LR, Anderson AW. Spatial normalization of the fiber orientation distribution based on high angular resolution diffusion imaging data. Magnetic Resonance in Medicine. 2009; 61:1520–1527. [PubMed: 19353649]
22. Irfanoglu MO, Koay CG, Pajevic S, Machiraju R, Basser PJ. Nonlinear registration of diffusion mr images based on fiber bundles. MICCAI. 2009:181–189. [PubMed: 20425986]
23. Jayachandra M, Rehbein N, Herweh C, Heiland S. Fiber tracking of human brain using fourth-order tensor and high angular resolution diffusion imaging. Magnetic Resonance in Medicine. 2008; 60:1207– 1217. [PubMed: 18958858]
24. Jian B, Vemuri B. A unified computational framework for deconvolution to reconstruct multiple fibers from diffusion weighted mri. IEEE Trans Med Imaging. 2007; 26(11):1464–1471. [PubMed: 18041262]
25. Kreher BW, Schneider JF, Mader I, Martin E, Hennig J, Il'yasov KA. Multitensor approach for analysis and tracking of complex fiber configurations. Magnetic Resonance in Medicine. 2005; 54(5):1216–1225. [PubMed: 16200554]
26. Krivanek, J.; Konttinen, J.; Pattanaik, S.; Bouatouch, K.; Zara, J. Fast approximation to spherical harmonic rotation. International Conference on Computer Graphics and Interactive Techniques; 2006.
27. Leow AD, Zhu S, Zhan L, McMahon K, de Zubicaray GI, Meredith M, Wright MJ, Toga AW, Thompson PM. The tensor distribution function. Magnetic Resonance in Medicine. 2009; 61:205–214. [PubMed: 19097208]
28. Li H, Xue Z, Guo L, Wong ST. Simultaneous consideration of spatial deformation and tensor orientation in diffusion tensor image registration using local fast marching patterns. Information Processing in Medical Imaging. 2009:63–75. [PubMed: 19694253]

29. Qazi AA, Radmanesh A, O'Donnell L, Kindlmann G, Peled S, Whalen S, Westin C-F, Golby AJ. Resolving crossings in the corticospinal tract by two-tensor streamline tractography: Method and clinical assessment using fmri. NeuroImage. 2009; 47:T98–T106. [PubMed: 18657622]
30. Ritchie DW, Kemp GJL. Fast computation, rotation, and comparison of low resolution spherical harmonic molecular surfaces. Journal of Computational Chemistry. 1999; 20(4):383–395.
31. Schultz T, Seidel H-P. Estimating crossing fibers: A tensor decomposition approach. IEEE Trans Visualization and Computer Graphics. Nov-Dec;2008 14(6):1635–1642.
32. Thirion J. Image matching as a diffusion process: an analogy with maxwell's demons. Medical Image Analysis. 1998; 2:243–260. [PubMed: 9873902]
33. Tuch DS. Q-ball imaging. Magnetic Resonance in Medicine. 2004; 56:1358–1372. [PubMed: 15562495]
34. Tuch DS, Reese TG, Wiegell MR, Wedeen VJ. Diffusion mri of complex neural architecture. Neuron. 2003; 40(5):885–895. [PubMed: 14659088]
35. Tuch, D.; Weisskoff, R.; Belliveau, J.; Wedeen, V. High angular resolution diffusion imaging of the human brain. Proceedings of the 7th Annual Meeting of ISMRM; 1999. p. 321
36. Vercauteren T, Pennec X, Malis E, Perchant A, Ayache N. Insight into efficient image registration techniques and the demons algorithm. Information Processing in Medical Imaging. 2007:495–506. [PubMed: 17633724]
37. Vercauteren T, Pennec X, Perchant A, Ayache N. NeuroImage. 2009; 45:s61–S72. [PubMed: 19041946]
38. von dem Hagen E, Henkelman R. Orientational diffusion reflects fiber structure within a voxel. 2002:454–459.
39. Wedeen VJ, Hagmann P, Tseng WYI, Reese TG, Weisskoff RM. Mapping complex tissue architecture with diffusion spectrum magnetic resonance imaging. Magnetic Resonance in Medicine. 2005; 54:1377–1386. [PubMed: 16247738]
40. Wu YC, Field AS, Alexander AL. Computation of diffusion function measures in q-space using magnetic resonance hybrid diffusion imaging. IEEE Trans on Med Imaging. Jun; 2008 27(6):858–865.
41. Yap PT, Wu G, Zhu H, Lin W, Shen D. Timer: Tensor image morphing for elastic registration. NeuroImage. 2009; 47:549–563. [PubMed: 19398022]
42. Yeo BT, Vercauteren T, Fillard P, Peyrat JM, Pennec X, Golland P, Ayache N, Clatz O. Dt-refind: Diffusion tensor registration with exact finite-strain differential. IEEE Trans Med Imaging. 2009; 28(12):1914–1928. [PubMed: 19556193]
43. Zhan W, Gu H, Xu S, Silbersweig DA, Stern E, Yang Y. Circular spectrum mapping for intravoxel fiber structures based on high angular resolution apparent diffusion coefficients. Magnetic Resonance in Medicine. 2003; 49(6):1077–1088. [PubMed: 12768586]
44. Zhan W, Stein EA, Yang Y. Mapping the orientation of intravoxel crossing fibers based on the phase information of diffusion circular spectrum. NeuroImage. 2004; 23(4):1358–1369. [PubMed: 15589100]
45. Zhang H, Avants BB, Yushkevich PA, Woo JH, Wang S, McCluskey LF, Elman LB, Melhem ER, Gee JC. Highdimensional spatial normalization of diffusion tensor images improves the detection of white matter differences: An example study using amyotrophic lateral sclerosis. IEEE Trans Med Imaging. 2007; 26(11):1585–1597. [PubMed: 18041273]
46. Zhang H, Yushkevich PA, Alexander DC, Gee JC. Deformable registration of diffusion tensor mr images with explicit orientation optimization. Medical Image Analysis. 2006; 10(5):764–785. [PubMed: 16899392]

Appendix

The rotation matrix about a unit length vector $< u, v, w >$ by angle α has the following form:

$$\mathrm{R}=\begin{bmatrix} u^2+(v^2+w^2)\cos\alpha & uv(1-\cos\alpha)-w\sin\alpha & uw(1-\cos\alpha)+v\sin\alpha \\ uv(1-\cos\alpha)+w\sin\alpha & v^2+(u^2+w^2)\cos\alpha & vw(1-\cos\alpha)-u\sin\alpha \\ uw(1-\cos\alpha)-v\sin\alpha & vw(1-\cos\alpha)+u\sin\alpha & w^2+(u^2+v^2)\cos\alpha \end{bmatrix} \quad (18)$$

We get

$$\begin{gathered} R(2,1)-R(1,2)=2w\sin\alpha, \\ R(1,3)-R(3,1)=2v\sin\alpha, \\ R(3,2)-R(2,3)=2u\sin\alpha, \end{gathered}$$

$$\begin{gathered} (R(2,1)-R(1,2))^2 \\ +(R(1,3)-R(3,1))^2 \\ +(R(3,2)-R(2,3))^2 \\ =4\sin^2\alpha(u^2+v^2+w^2)=4\sin^2\alpha \end{gathered}$$

$$\begin{gathered} |\cos\alpha|=0.5(4-4\sin^2\alpha)^{\frac{1}{2}} \\ =0.5(4-((R(2,1)-R(1,2))^2+(R(1,3)-R(3,1))^2+(R(3,2)-R(2,3))^2))^{\frac{1}{2}} \end{gathered}$$

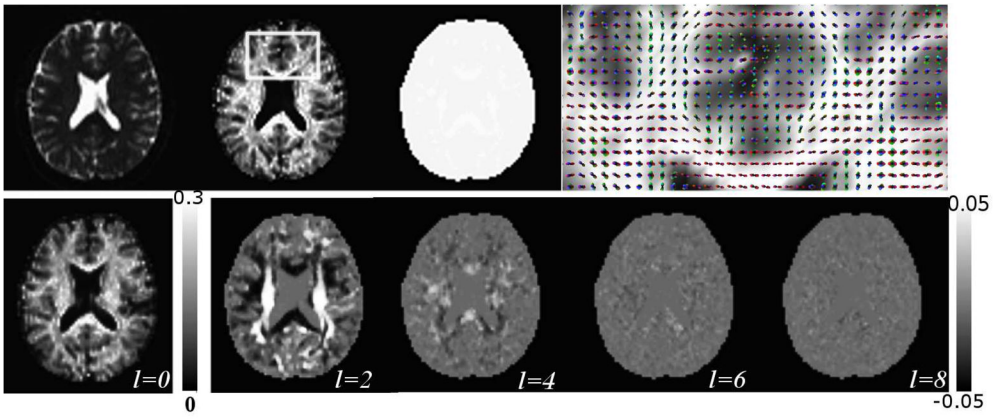

Fig. 1.

An example of reconstructed ODF data set represented by SH coefficients. Top row from left to right: B0 image at b=0; the L^2 norm of the ODF map; the L^2 norm of the normalized ODF map; the enlarged ODF shapes within the box region. Bottom row from left to right includes the SH coefficients at $l = 0, m = 0$; $l = 2, m = 0$; $l = 4, m = 0$; $l = 6, m = 0$; and $l = 8, m = 0$.

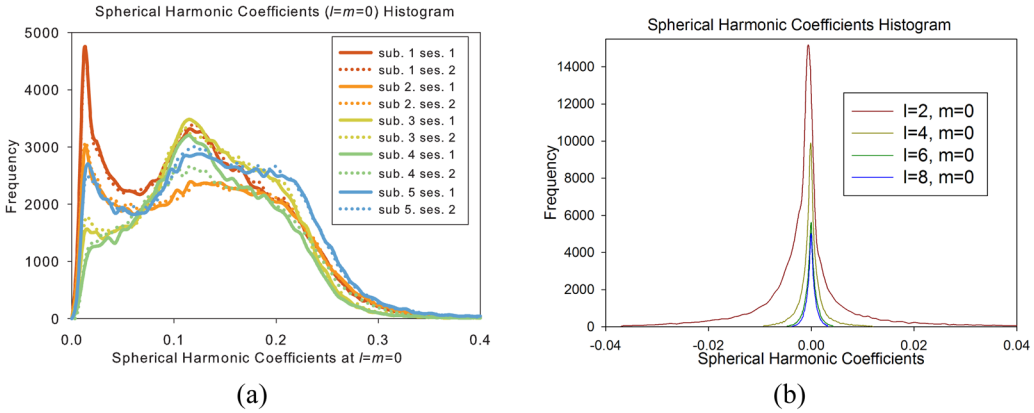

Fig. 2.

The histograms of ODF SH coefficients. Note in (a), one color represents one subject, solid and dotted lines denote two sessions from the same subjects.

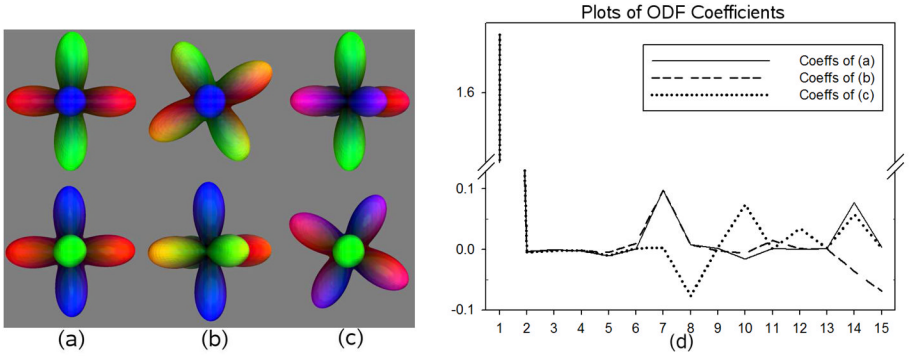

Fig. 3.

Illustration of the ODF reorientation with simulated mixed 3-tensor data sets. (a) the original ODF projected on the *xy* plane on the top and the *xz* plane at the bottom. (b) the ODF rotated 30° along the *z*-axis. (c) the ODF rotated 30° along the *y*-axis. (d) The plots of corresponding ODF coefficients stored in a 1*D* array $[c_0^0, c_{-2}^2, c_{-1}^2 \cdots, c_3^4, c_4^4]$. The color encoding follows the conventional scheme: red for the direction of left-right, green for anterior-posterior and blue for superior-inferior.

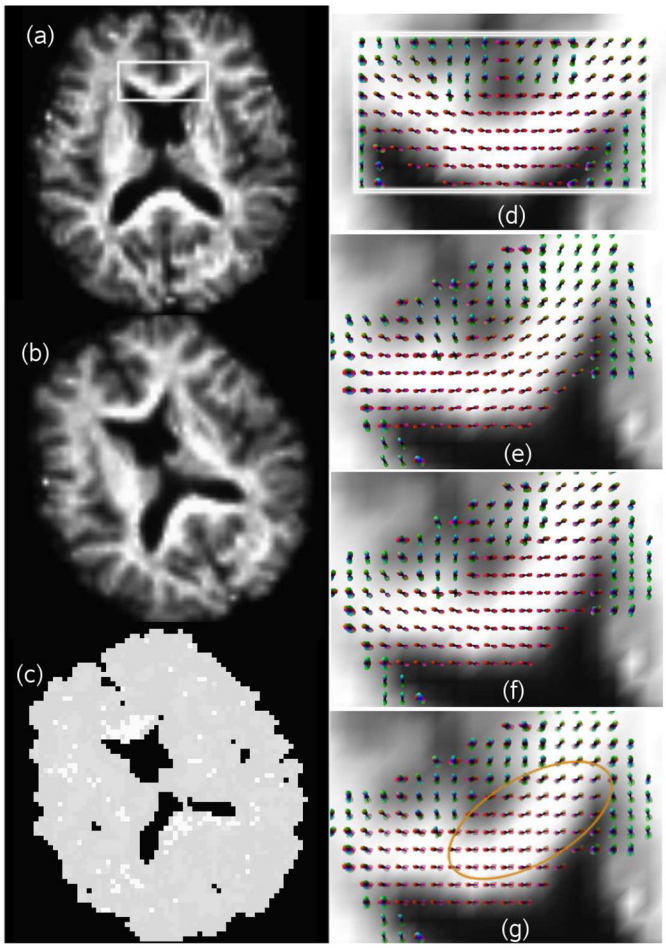

Fig. 4.

Illustration of ODF reorientation using real diffusion data with a 25° rotation along the *z*-axis. (a) the original ODF map represented using SH coefficient at $l = m = 0$. (b) the rotation ODF map. (c) the directional consistency map between the reoriented and non-reoriented ODF maps with a color scale from 0 to 1, and masked by thresholding the zero order coefficients at 0.1. (d) the enlarged original ODFs, (e) the ODFs with reorientation, and (f) without reorientation on the rotated ODF map, and (g) ODFs with and without reorientation overlaid on each other. The circled region shows visible directional inconsistency between with and without ODF reorientation.

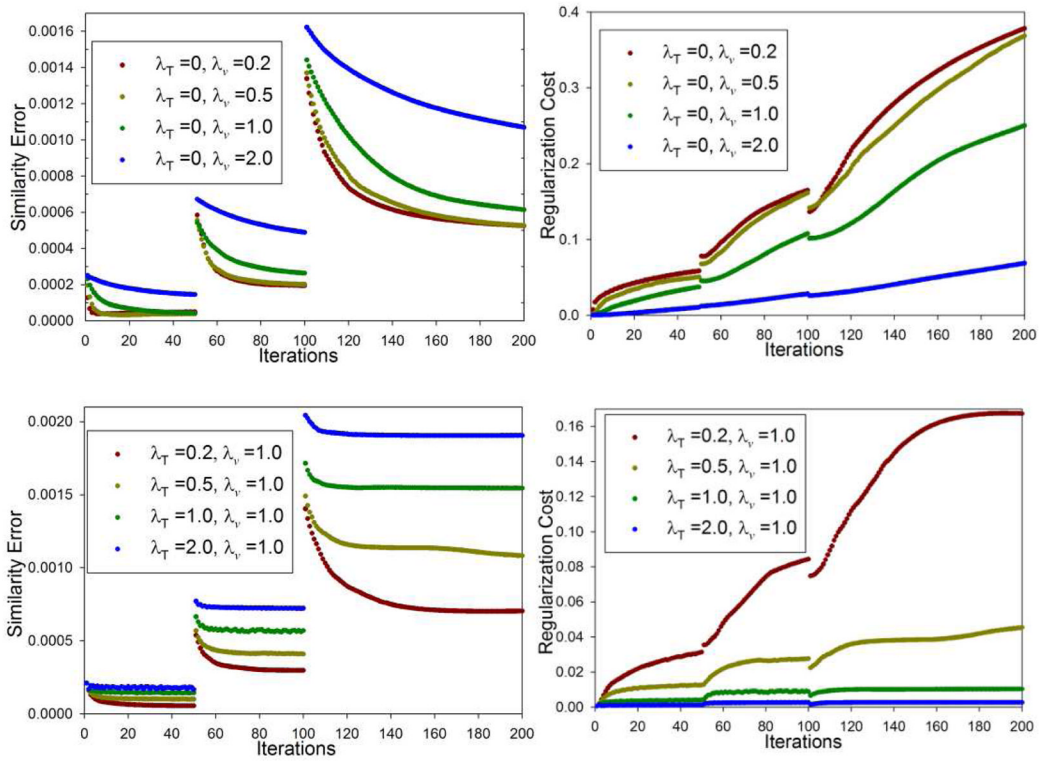

Fig. 5.

Plots of similarity error and regularization costs under different regularization parameter settings. A multi-resolution scheme was used during the registration. The number of iterations were set to 50 for two lower resolutions and 100 for the full resolution. The discontinuity in the plots is due to the multi-resolution approach.

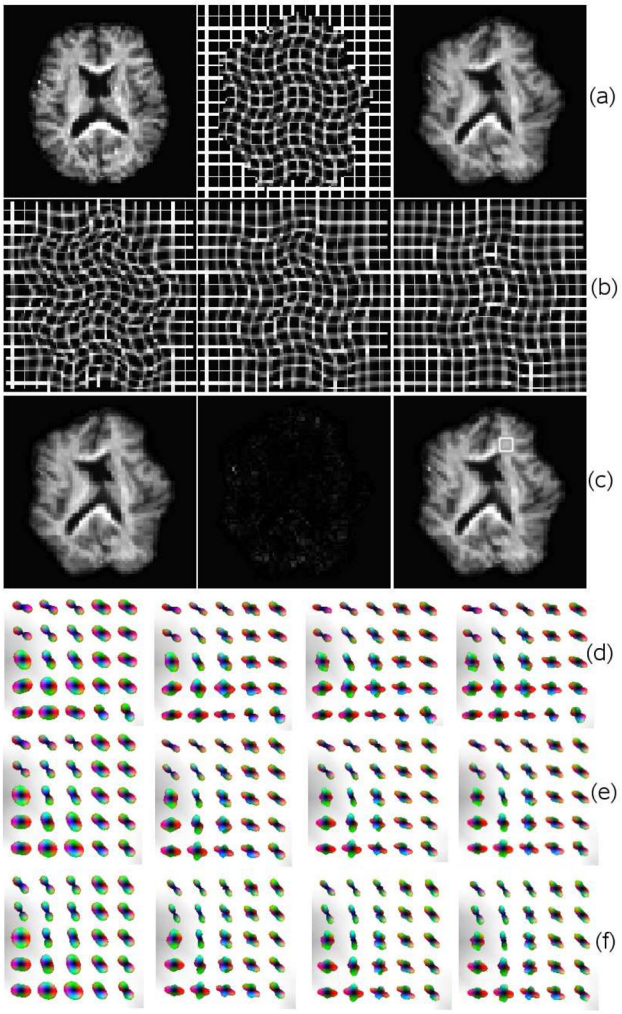

Fig. 6.

ODF Registration of the simulated ODF maps. From left to right: (a) a real ODF map, the simulated transformation field and the deformed ODF using the simulated transformation serving as the reference; (b) estimated transformations using $\lambda_T = 0$, $\lambda_v = 0.5$, $\lambda_T = 0.5$, $\lambda_v = 1.0$ and $\lambda_T = 1.0$, $\lambda_v = 1.0$; (c) deformed, the difference between the deformed and reference and the reference ODF maps; (d) the reference ODF shapes in the box region with $L = 2, 4, 6, 8$; (e) ODF shapes after registration in the same region with $L = 2, 4, 6, 8$; (f) ODF shapes after registration without ODF reorientation.

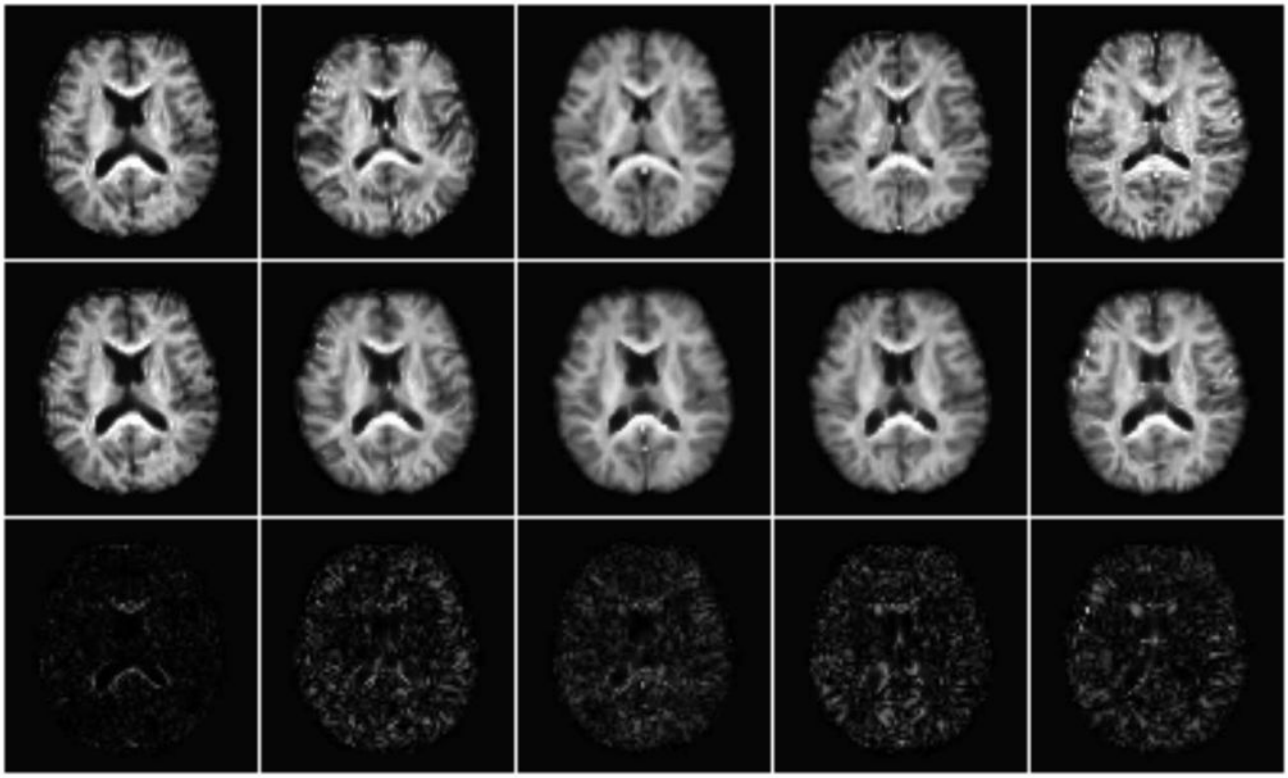

Fig. 7.

ODF registration results after diffeomorphic registration using SHs with $L = 4$. The top row from left to right: the affine aligned ODF maps represented using the norm of the SH coefficients for the reference, and four other subjects' data. The second row from left to right: the reference ODF map, and the four deformed ODF maps (with the same order as the top row) to the reference. The third row from left to right: the absolute difference of the L^2 norm of the SH coefficients between the reference and the data from the same subject in a different session, the difference between the reference and the four deformed ODF maps.

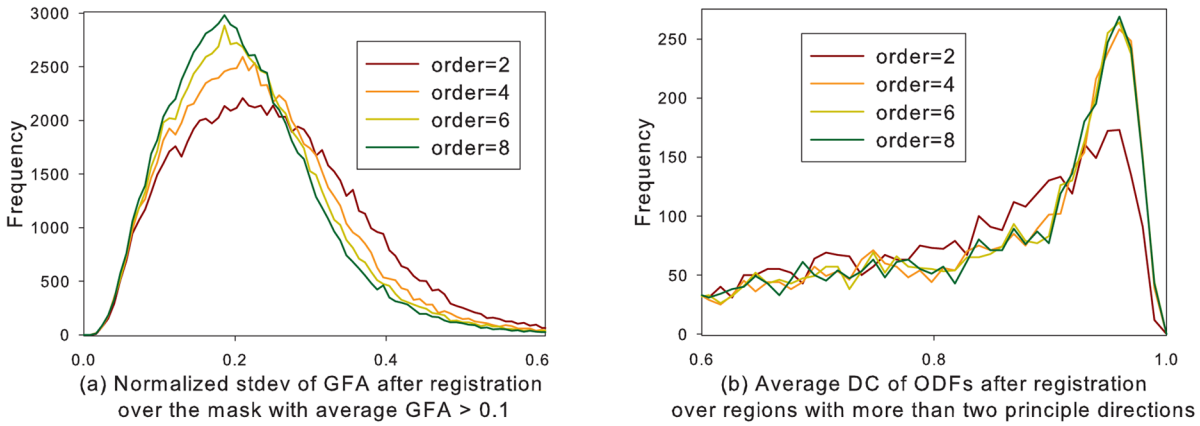

Fig. 8.

Histograms of the normalized standard deviation of GFA and average DC after diffeomorphic registrations using SHs with $L = 2, 4, 6, 8$.

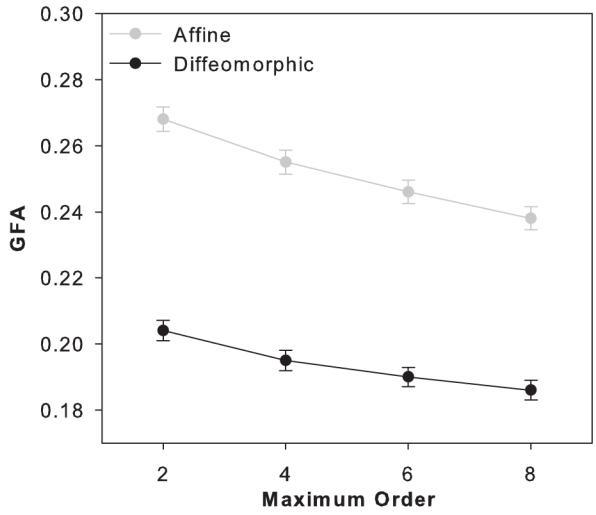

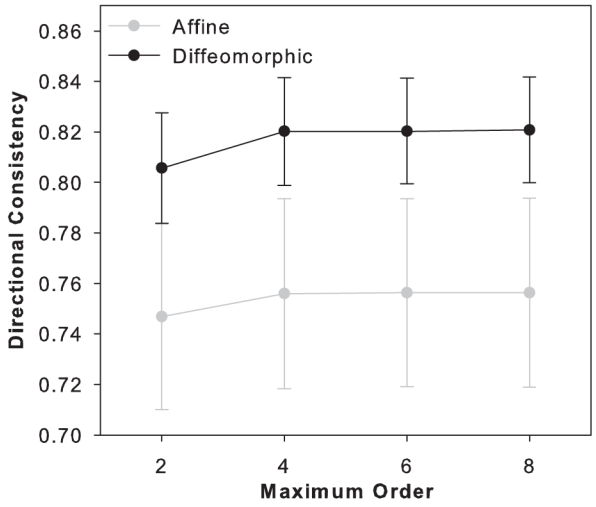

Fig. 9.
Plots of the average GFA and DC in affine and diffeomorphic registration with different maximum orders of SHs.

TABLE I

Registration Performance in the simulation experiment evaluated using the average field distance, normalized standard deviation of GFA and directional consistency.

metric	L=2	L=4	L=6	L=8
field dist	0.4997	0.4965	0.4962	0.4959
nstd GFA	0.1353	0.1312	0.1284	0.1269
DC	0.8667	0.8747	0.8765	0.8784